Optical and structural characterization of CeO2/B4C multilayers near boron K-edge energy

M.G. Sertsu[1,2,5*], A.Giglia[3], S.Brose[6], A.Comisso[1,2] , Z.S. Wang[4], L.Juschkin[5] , P. Nicolosi[1,2]

[1] University of Padova, Department of Information Engineering, via Gradenigo 6B, 35131 Padova, Italy

[2] Institute for Photonics and Nanotechnologies Laboratory for Ultraviolet and X-ray Optical Research, via Trasea 7, 35131, Padova, Italy

[3] CNR- Istituto Officina Materiali, I-34149 Trieste, Italy

4 Tonji University, China

[5] RWTH Aachen University, Experimental Physics of EUV, Steinbachstr. 15, 52074 Aachen, Germany

[6] RWTH Aachen University, Chair for the Technology of Optical Systems (TOS), Steinbachstr. 15, 52074 Aachen, Germany

ABSTRACT

A search for novel materials for making multilayers of high reflectivity has been driven by the vigorous demand towards miniaturizing photonics. A typical consumer of high performance multilayers (MLs) is the extreme ultraviolet lithography (EUVL) based on the 13.5 nm laser produced plasma (LPP) source. To sustain "Moore's law" and print fine features below 10 nm on integrated circuits (IC), source of radiation for the EUVL has to shift towards even shorter wavelengths where 6.x nm wavelength seems to be immediate successor. However, the 6.x nm EUV lithography needs MLs of reflectivity performance above 70 % to support high volume manufacturing (HVM). It is clear that more work is required particularly on the development of MLs with high reflectance, stable to thermal heat and sufficient lifetime. In this work new MLs of B4C/CeO2 are deposited, analyzed and characterized for the first time. Combinations of X-ray reflectometry (XRR) and EUV reflectance measurements near resonance edge of boron are analyzed to derive structural and optical parameters of MLs. ML coatings of B4C/CeO2 MLs have shown similar reflectance performance with the leading candidate MLs around 6.x nm wavelength. Analysis shows that interlayer diffusion is a major reason for low reflectivity performance. Cross-sectional scanning electron microscopy (SEM) images of the MLs have proved formation of interlayer diffusion.

Keywords: EUV multilayers, B4C films, CeO2 thin films, EUV lithography, 6.x nm EUVL, multilayer interfaces, ML EUV reflectivity, and genetic algorithm

1. INTRODUCTION

Multilayers are key components in several areas of EUV and X-ray optics. Chromium-Scandium (Cr/Sc) and alloy-ceramic oxide multilayers of $Ni_{80}Nb_{20} - MgO$ are among popular candidates for soft X-ray microscopy in the "water-window" [1, 2]. Si/Mo, Si/Ir and Si/Mg multilayers have been incorporated as EUV imaging components for space mission telescopes particularly in the 17-30.5 nm wavelength regime [3]. Applications as polarizers, beam splitters, narrow and broadband filters in the EUV and soft X-ray are also popular in optical engineering [4]. Another eminent application of MLs in the EUV lithography as high throughput reflectors and beam shapers has gained a reputation of sustaining "Moore's Law" in the semiconductor industry, that empirically stated that number of transistors in a microprocessor-chip doubles every 18 months [5]. The EUV lithography utilizes a plasma radiation source at 13.5 nm, which enables semiconductor manufacturers to print circuit lines at or below the 22 nm node. As current microlithography based on 193 nm ArF laser source is already challenged by physical and/or economical limits, EUVL has gained momentum as a major contender for next generation lithography by the semiconductor industry. A leading company in the EUVL development is ASML followed by many other contenders such as IBM, INTEL and others. ASML's NXE-series EUV scanners have printed 1000 wafers/day [SPIE 2015, San Jose].This approaches the industry high volume manufacturing demand, which lies about 1600 wafers/day. The output power of LPP sources, contamination and lifetime issues of collector mirrors, spatial and temporal stability of plasma pulses need to be improved to meet requirements of high volume manufacturing.

In the meantime, there is a growing interest to shorter wavelength EUV lithography platform, which is commonly known as "Beyond EUV" lithography (BEUV). The motivation behind BEUV lithography (BEUVL) at 6.x nm is to sustain "Moore's law" and paving the way towards printing below 10 nm feature sizes on IC. For lithographic systems, wavelength and numerical aperture (NA) determine the smallest printable feature size according to equation (1):

$$\text{Smallest feature} = k_1 \frac{\lambda}{NA} \tag{1}$$

Where k_1 is a constant largely dominated by the optical system, lithographic processes, and photoresist recording and processing.

Decreasing k_1, increasing NA, and lower wavelength λ are necessary for printing finer patterns on Si wafer. Both k_1 and NA are, however, challenged by theoretical and engineering limits. Therefore, utilization of LPP sources at shorter wavelengths such as 6.x nm may sustain "Moore's law''. Reports show the possibility of extending EUV lithography to 6.x nm from the standard 13.5 nm EUVL [6, 7]. Gadolinium (Gd) and Terbium (Tb) fuels for LPP sources producing ($\sim 1\ kW$) at the intermediate focus (IF), optical system with 40% collection efficiency, ~5% conversion efficiency at 2% bandwidth, and 58 % ML reflectivity have been reported [8]. The ML performance clearly shows that more work needs to be done to reach minimum reflectivity requirement of 70% for the new BEUVL platform. In response to this ML demand, B4C based MLs such as La/B4C, LaN/B4C and LaN/B have shown better performances [9-11].In this work, new ML combinations are designed, deposited and characterized for reflectance performance at the 6.x nm wavelength. Cerium oxide (CeO2) and Boron carbide (B4C) combinations are investigated in this work. Theoretical analysis show that CeO2/B4C MLs have comparable performance with the leading candidates (Fig 1).

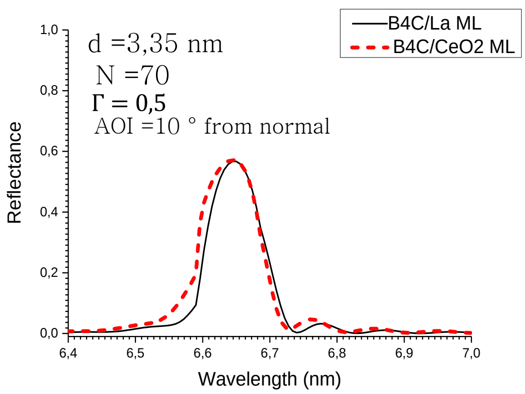

Figure 1: Theoretical reflectivity performances of top candidate MLs in the 6.x nm wavelength.

A preliminary analysis of CeO2/B4C MLs for the first time deposited by DC magnetron sputtering is performed. Here, we present ML reflectivity performance at the working wavelengths of 6.x (near the boron edge), period and layer thicknesses, and optical properties of layers and interlayers.

1.1 Reflectivity models for multilayer structures

One of the models for reflectivity calculations from multilayer structures is the Parratt's method [12]. Parratt's method assumes continuity of electric field vector ($\mathbf{K_Z}$) in the perpendicular direction to the ML. For a generalized multilayer structure shown in Fig 1, layer j has a thickness t_j and complex refractive index n_j. In the soft X-ray region, the complex refractive index is given by

$$n_j = 1 - \delta_j - i\beta_j \tag{2}$$

Where δ_j and β_j are real values and in the order of $\cong 10^{-3}$ for most elements.

A plane electromagnetic field E propagating in a homogeneous medium of refractive index n can be solved by Helmholtz equation.

$$(\nabla^2 + \boldsymbol{k}^2)E = 0 \tag{3}$$

Where $k = (2\pi n)/\lambda$ is modulus of wave vector k and ∇ is the Laplacian operator.

For photon energies above 30 eV, the interaction of the electromagnetic wave with individual atoms dominates the general interaction with the condensed system. Therefore, total scattering in the system can be approximated as a sum of scattered amplitudes from each individual atom [13, 14]. For EUV and soft X-ray regime, δ and β are parametrized in terms of the scattering factors (eqs 4 and 5) [14]. Note however that due to the high sensitivity to local atom interactions and to slight optical fluctuations, these equations might not be valid at near absorption edge energies.

$$\delta \cong \frac{r_e}{2\pi}\frac{N_A}{M}\rho\ \lambda^2 f_1 \tag{4}$$

$$\beta \cong \frac{r_e}{2\pi}\frac{N_A}{M}\rho\ \lambda^2 f_2 \tag{5}$$

Where f_1 and f_2 are real and imaginary components of the complex scattering factor f, N_A is Avogadro's constant$\approx 6.022 \times 10^{23}\ mol^{-1}$, r_e is the classical electron radius ($\sim 2.82 \times 10^{-15}\ m$), ρ is mass density and M is the molar mass.

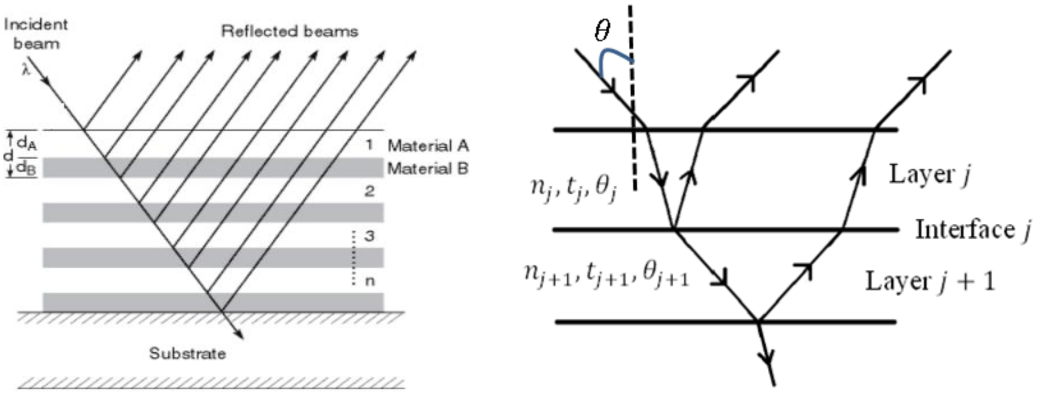

Figure 2: Schematic of multilayer structure, θ is the incidence angle measured from normal at the top layer, and θ_j is a complex direction of propagation in the j^{th} layer [15]

Fresnel reflection coefficient, for S-polarized radiation, from an interface lying between layers j and $j+1$ is given by:

$$r^s_{j,j+1} = \frac{n_j\, cos\theta_j - n_{j+1}\, cos\theta_{j+1}}{n_j\, cos\theta_j + n_{j+1}\, cos\theta_{j+1}} \tag{6}$$

In similar manner, Fresnel coefficient for p-polarized radiation is calculated by eqn (4)

$$r^p_{j,j+1} = \frac{n_j\, cos\theta_{j+1} - n_{j+1}\, cos\theta_j}{n_j\, cos\theta_{j+1} + n_{j+1}\, cos\theta_j} \tag{7}$$

Parratt's method calculates the total reflected amplitude ζ_j from the j^{th} interface using a recursive relation, eq (5).

$$\zeta_j = \frac{r_{j,j+1} + \chi_{j+1} exp(-i2\varphi_{j+1})}{1 + r_{j,j+1}\chi_{j+1} exp(-i2\varphi_{j+1})} \tag{8}$$

Where $\varphi_j = \frac{2\pi}{\lambda} t_j n_j\, cos\theta_j$.

Because Parratt's method assumes semi-infinite substrate thickness, reflection from the bottom structure (i.e. substrate) is zero. Loss of reflectivity due to interfacial roughness and diffuseness can be accounted in equation (8) by multiplying Fresnel coefficients at each interface by the preferred interface profile functions.

1.2 Numerical fit models for multilayer reflectance

Reconstruction of ML parameters from reflectivity measurement is an inverse process and thus model dependent. Equation 5 implicitly contains all the structural and optical parameters of a ML that need to be determined through a nonlinear curve fit. Gradient-expansion algorithms such as Marquardt and Levenberg-Marquardt (LMA) are popular in ML parameter estimation by trying to fit a model of nonlinear function to measured reflectivity. The curve fitting is performed by iteratively tuning each parameter against a χ^2 test. The χ^2 is a goodness of fit value similar to Pearson's criterion [16].

$$\chi^2 = min\left(\frac{\sum_i^N (I_i^{calc} - I_i^{meas})^2}{\sum_i^N I_i^{meas}}\right) \tag{9}$$

Where N refers to number of measured data points, and the denominator represents a normalized statistical weighting.

Gradient based and/or Gauss-Newton algorithms such as LMA often retrieve few parameters of a ML or parameters of just a single film with a reasonable convergence. However, reconstruction of multiple optical and structural parameters of MLs demands a robust algorithm than LMA and/or any other gradient-expansion based iterative algorithms [17].

In this work, Genetic algorithm (GA) and a more complex form of it known by differential algorithm (DE) are alternatively used for ML parameters fitting. Detail description of the GA has been published in [18]. Here basic principles important for ML structure retrieval through fitting are discussed.

Inspired by Darwinian 'survival of the fittest' theory in the biological selection process, GA is now implemented in several physical sciences and engineering optimization problems. GA is considered as a global optimization algorithm because it is generally less sensitive to the choice of initial parameter values and less susceptible to stacking at local minima even if the function contains more than one peak [18]. GA in contrast to other methods combine a stochastic search of global minima in a parameter space with intelligent strategy of solution finding [17]. A descriptive flowchart for Genetic algorithm is given in Figure 3.

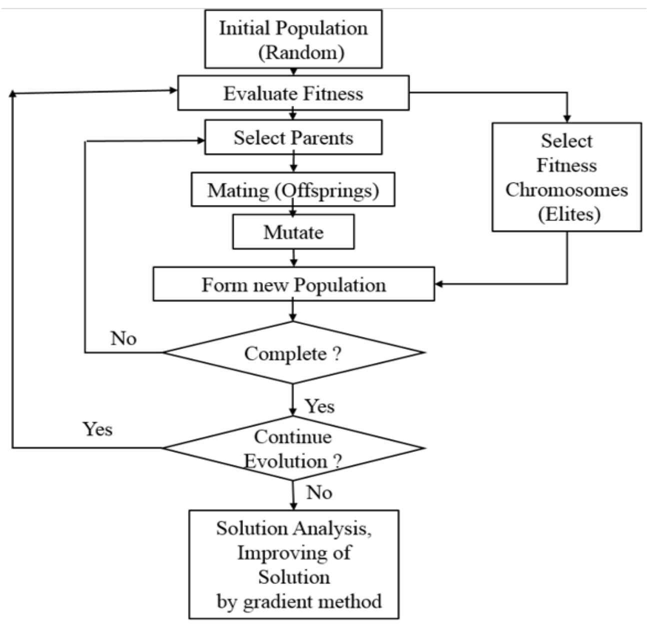

Figure 3: Basic flow chart of genetic algorithm

In the case of both GA and DE algorithms, a figure of merit (FOM) is given in same way as the χ^2 statistic for gradient-based algorithms.

$$\mathrm{FOM} = \frac{\sum_{i=1}^{N} w(i)[I^{calc}(i) - I^{meas}(i)]^n]}{\sum_{i=1}^{Nmeas} w(i)} \qquad (10)$$

Where $w(i)$ is the weighting factor for each population and n is a positive integer number fixed by the user.

Each individual of each generation is tested against the FOM to pass on to the population of next generation. One more step in the GA is separation of best individuals, elites, based on their fitness to the FOM, and directly transferring them to the new generation. This prevents from losing best solutions that have been found at earlier generations. The process continues until a certain number of generations are reached or FOM reaches a certain minimum value fixed by the user.

2. EXPERIMENT, SAMPLE DESCRIPTION AND DATA PROCESSING

The potentiality of using near edge EUV reflectivity measurements in combination with X-ray reflectivity (XRR) to improve analysis and characterization of buried interfaces of ML structures has been discussed in recent papers [19-21]. There, the measurements were designed in such a way that structural and optical properties of MLs can be derived with precision, simplicity, reliability and consistency. An innovative extension of this experimental method is deployed here to characterize a new ML's optical and structural parameters.

In this work, measurements of at-wavelength grazing incidence EUV reflectivities (GI-EUVR) were carried out at the BEAR (Bending magnet for Emission, Absorption and Reflectivity) beam line, ELETTRA Synchrotron in Trieste [22]. The stability and reproducibility of the synchrotron source, working in top-up mode, the monitoring setup of the incoming beam intensity and the high control of the beam-line experimental setup, allowed to get reliable experimental data with a SNR of 0.5%. On the other hand XRR measurements have been done at Cu K_α line energy (8047 eV) for $2\theta - \omega$ scan of the X'PERT-PRO diffractometer system. Cross-sectional scanning electron microscopy (SEM) is performed at the Helmholtz Nanoelectronic Facility of the Research Centre Jülich.

In the present experiment, two B4C/ CeO2 ML samples (Table 1) were measured for EUV and X-Ray reflectivities. The layer systems were deposited by DC magnetron sputtering techniques. The first sample, Sample_01, was designed for high reflectance performance at 6.x nm EUV and 10° incidence angle from normal. The second sample, Sample_02 was measured for a grazing incidence EUV reflectivity (GI-EUVR). GI-EUVR is a sensitive method that accounts the correlation between optical and structural parameters of MLs during numerical fitting with a reasonable accuracy, and can be reliable in deriving ML parameters. X-ray reflectivity (XRR) measurements have been done for both samples to determine period and density of the MLs. Period and layer thicknesses of Sample_02 obtained by fitting to measured GI-EUVR are compared with high resolution cross-sectional scanning electron microscopy (SEM) image of Sample_02 to check reliability of the method.

Table 1: ML design parameters. Note that Γ is the ratio of bottom layer (CeO2 layer) to the period of MLs.

ML types	Design parameters
Sample_01: B4C/CeO2	d=35 A°, $t_{CeO2} = 16\,A°, t_{B4C} = 19$ Å, N= 40, $\Gamma = 0.457$
Sample_02: B4C/CeO2	d=200 A°, $t_{CeO2} = 80$ A°, $t_{B4C} = 120$ A°, N= 10, $\Gamma = 0.4$
Substrate	Si

To retrieve optical and structural parameters of the MLs, a nonlinear curve fit to measured XRR and GI-EUVR data in IMD software package [23] are performed. IMD is a software package that can be used to calculate both specular and non-specular (diffuse) optical functions (e.g., reflectance, transmittance, scattering, etc.) of an arbitrary multilayer. High depth spatial resolution due to short XRR wavelength ($\approx 1.5407A°$) allows to determine the period (d) of MLs with less than $3A°$ error [24]. Reports in [14, 21, 25] show that a combined analysis of XRR and near normal EUVR give accurate reconstruction of ML parameters. In this paper, measurement of GI-EUV reflectance near boron K edge (183.84 eV) is done to check its potential for the first time in reconstructing both structural and optical properties of a ML. This GI-EUVR analysis method is tested against the relatively well-known XRR and near normal EUVR methods.

3. RESULTS AND DISCUSSION

Measured and calculated EUV reflectivity at 10° from normal incidence for Sample_01 is given in Fig 2.

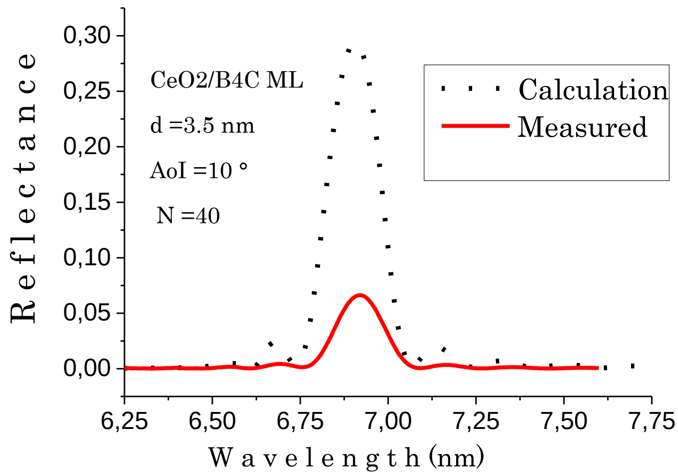

Figure 2: Calculated and measured curves for Sample_01. For calculations tabulated values of δ and β are taken [ref: CXRO database].

The measured reflectivity performance at 10° from normal is nearly 6.65 %. This is approximately 4.4 times less than the theoretical reflectance but it is equivalent to La/B ML performance at 6.x nm wavelength [26]. A fit to the XRR curve at the $CuK_{\alpha1}$ edge and retrieved parameters are shown in Fig 3 and Table 2 respectively.

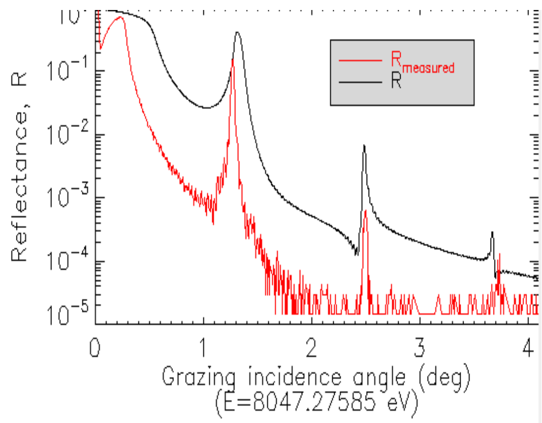

Table 2: Resulting ML parameters from XRR fit of Sample_01

t_{B4C} (Å)	21.596
t_{CeO2} (Å)	14.869
d (Å)	36.464
Γ – ratio	0.408
ρ_{CeO2} ($\frac{gm}{cm3}$)	5.520
ρ_{B4C} ($\frac{gm}{cm3}$)	2.719

Figure 3: Nonlinear curve fit (black) in IMD to measured XRR (red color) data for Sample_01 at the $CuK_{\alpha 1}$ line. Table 2 at the right contains thickness and density parameters of the ML obtained from the fit.

Fitting of XRR data for Sample_01 gives densities of CeO2 and B4C to be 8.085 and 2.98 gm/cm3 respectively. These values are far from the bulk values. Then, table 2 simply shows the low sensitivity of XRR measurement to density of MLs, which is directly, related to the optical constants via eqns 4 and 5. The $\Gamma -$ ratio is changed from a design value of 0.457 to 0.408 that can be associated to the variations of grazing incidence reflectivity due to the formation of interdiffusion layers [27]. However, one can count on XRR fit for a relatively correct value of period thickness due to the high spatial resolution of short X-ray wavelength (1.54 Å).

To investigate further optical and morphological parameters of the ML, nonlinear curve fit to measured data of EUV reflectance near the boron-edge (Fig 4) after introduction of interlayers is performed. At Boron edge, elemental and chemical sensitivities are higher are higher that can reconstruct accurate values. Table 3 contains thicknesses and optical constants of the ML obtained from the fitting at 10° of incidence from normal.

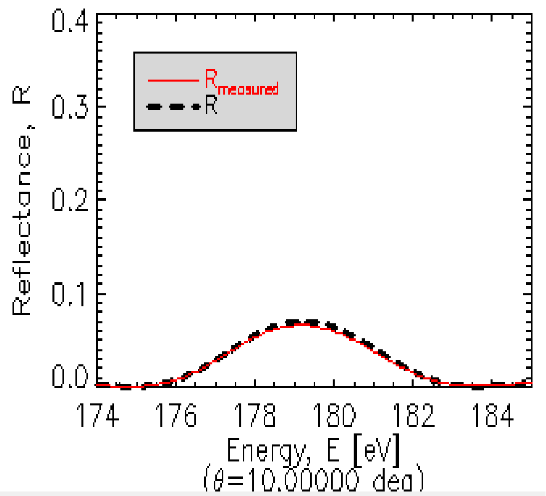

Table 3: ML parameters from EUVR fit for Sample_01

t_{B4C} (Å) = 10.068,	$\rho\ (\frac{gm}{cm3})$ = 2.537
Interlayer_01 (Å) =7.707,	$\rho\ (\frac{gm}{cm3})$ = 3.875
t_{CeO2} (Å) = 10.69,	$\rho\ \left(\frac{gm}{cm3}\right)$ = 5.103
Interlayer_02 (Å) = 7.095,	$\rho\ \left(\frac{gm}{cm3}\right)$ = 4.566
Period of ML d (Å)= 35.56	

Figure 4: Measured and fitted EUV reflectance for Sample_01 at 10° from normal incidence. Table 3 at the right side shows thickness and density parameters of the ML derived from numerical fit to measured EUV reflectance.

The density values looks reasonable when compared to bulk values and previous measurements [28, 29]. The period thickness from the EUV fitting (35.56 Å) is slightly Shorter than XRR fit which is a common difference from XRR. TO get better values, a combined analysis oft he XRR and near normal EUV are nowadays very common. However, here we wanted to test how accurate a GI-EUVR near boron edge can describe a ML. Retreived values are then compared to a SEM image.

As a proof of concept, an alternative at-wavelength metrology of EUV reflectance for characterizing optical and structural parameters of MLs is described here. Grazing incidence EUV reflectance measurements of Sample_02 (Table 1) at 183.84 eV (near Boron absorption edge) is given in Fig 5. This at-wavelength metrology is grazing incidence EUV equivalent of XRR. If fitted appropriately, GI-EUVR could reconstruct both optical and structural parameters accurately as reported in [25].

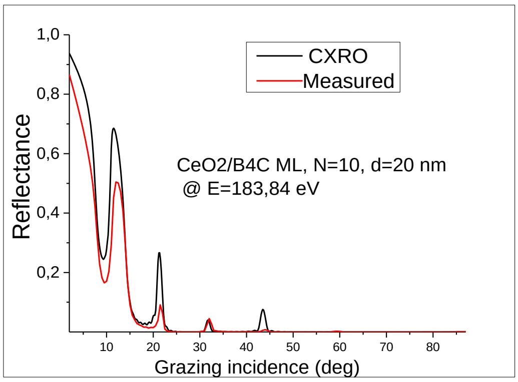

Figure 5: Measured and theoretical simulation of GI-EUV reflectance for Sample_2. Optical data (δ and β) for the theoretical simulation are taken from CXRO database.

Fitting parameters of Sample_02 as obtained from fits of XRR and GI-EUVR are given in Tables 4 and 5 respectively.

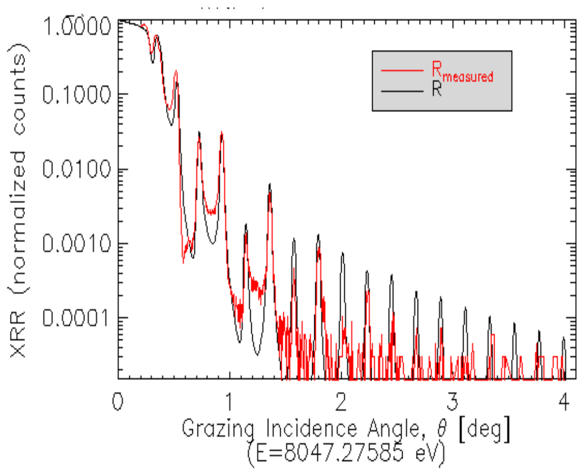

Table 4: ML parameters obtained from XRR fit of Sample_02

t_{B4C} (Å) = 116.623	
t_{CeO2} (Å) =83.057	
Period d (Å)= 199.68	
ρ_{CeO2} ($\frac{gm}{cm3}$)	7.065
ρ_{B4C} ($\frac{gm}{cm3}$)	2.84

Figure 6: Measured and calculated XRR curves for Sample_02 at the $CuK_{\alpha1}$ edge. Table 4 at the right shows thickness and density parameters of the ML as obtained from the XRR fit. Typical interface roughness of 5 Å is introduced in each interface during the fitting.

GI-EUVR fitting for Sample_02 to reconstruct both density and thickness is performed in differential algorithm (DE) to minimize the figure of merit (FOM) function. Parameters reconstructed from the fit are shown in Table 5, fitted curve is also given in Fig 7.

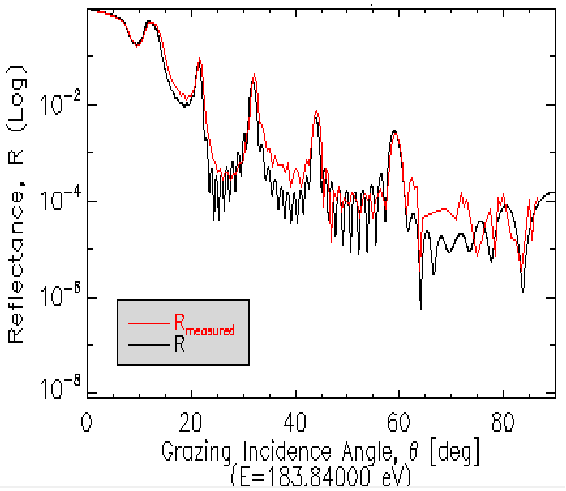

Table 5: Resulting ML parameters from EUVR fit of Sample_02

t_{B4C} (Å)~ 93.474,	$\rho\left(\frac{gm}{cm3}\right) = 2.523$
Interlayer_01 (Å) ~ 22.164,	$\rho\left(\frac{gm}{cm3}\right) = 5.257$
t_{CeO2} (Å)~ 57.638,	$\rho\left(\frac{gm}{cm3}\right) = 5.831$
Interlayer_02 (Å) ~ 25.455,	$\rho\left(\frac{gm}{cm3}\right) = 3.909$
Period of ML d (Å) ~ 198.732	

Figure 7: Measured and fitted GI- EUV reflectance for Sample_2 near the boron edge, 183.84 eV. Table 5 at the right shows thickness and density parameters of the ML as obtained from GI-EUVR fit. Colored layers show different layers and interlayers.

The period of the ML obtained from the GI-EUVR fit is 198.731 Å for Sample_02. This value is by 1.269 Å lower than design value and by 0.949 Å lower than the value obtained from XRR fit. Diffusion of B4C-on-CeO2 and CeO2-on-B4C created interlayers of different thicknesses. CeO2 being more diffusing than B4C, that might be due to a difference in thermal diffusion properties, gave rise to asymmetric interlayers. Effective average thickness of B4C-on-CeO2 interlayer is ~2.2 nm and that of CeO2-on-B4C interlayer is approximately 2.55nm. Reconstructed densities by fitting measured GI-EUVR data are as accurate as those derived through a combined analysis of XRR and near normal EUVR. This is demonstrates that at-wavelength analysis near the Boron K- edge (i.e. GI-EUVR near the Boron-edge) renders reliable and consistent optical ML properties. As a further test of the sample structure characteristics cross sectional TEM has been performed and results have been compared with those derived from the previously described analysis procedures. In fig 8 the SEM image for sample 2 is reported.

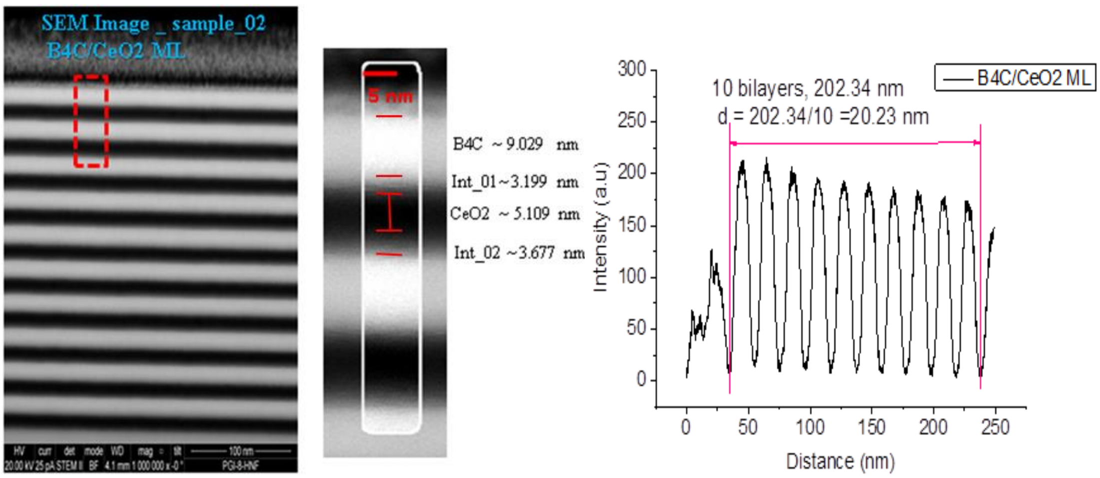

Figure 8: Scanning Electron Microscopy (SEM) image of Sample_02. Interface diffusion is clearly visible in the SEM image, which is a major cause for the low reflectivity performance. Int_01 refers to B4C-on-CeO2 interfacial diffusion and Int_02 is vice versa. On the right is periodic structures of the ML from which average period is calculated.

The presence of interdiffusion can be clearly observed which causes superposition of CeO2 and B4C atoms around the interfaces. This superposition might cause thickness profiles in the SEM image affected by a significant error [30]. A close look up into the onset in Fig 8 proves that the ambiguity to determine optical boundaries where real reflection takes place from the SEM image. The layer and interlayer thicknesses provided for a single period in Fig 8 are geometrical boundaries. If interlayer thicknesses are determined with some error from the SEM image, then all the other layer thicknesses contain certain errors because of the shading effect at the interfaces. Thus, one has to count on the fitting algorithm to determine the mean interface ("true thickness") and compare with the thicknesses from the SEM profile (Table 6). Thicknesses of a single period (2nd from top) in the SEM image are manually extracted with an approximate error of 5Å [31] by enhancing the contrast function among layers. Extracted thicknesses are put in column 2 of table 6 to make a rough comparison with fit results to GI-EUVR measured data.

Table 6: Parameters of Sample_02 obtained from SEM image and fitting to GI-EUVR measured data. Δ refers to difference between SEM and fitting values. The ratio column is just a division of SEM to GI-EUVR fit parameters. Interlayer_01 implies diffusion of B4C onto CeO2, and Interlayer_02 is the opposite.

ML parameter	SEM image	GI-EUVR fit	$\Delta(x_{SEM} - x_{GI-EUVR})$	ratio $(x_{SEM}/x_{GI-EUVR})$
t_{B4C} (Å)	90.29	93.474	-3.184	0.966
Interlayer_01 (Å)	31.992	22.164	9.828	1.4434
t_{CeO2} (Å)	51.093	57.638	-6.545	0.8864
Interlayer_02 (Å)	36	25.455	11.315	1.4445
$d_{average}$ (Å)	202.339	198.732	11.418	1.05745

In Table 6, thicknesses retrieved from fit of GI-EUVR and SEM image are significantly different. "True" thicknesses from SEM image can be obtained either by software processing of the image itself or relying on a robust fitting algorithm that independently determine thicknesses. In our case, we choose the latter based on a robust GA optimization supplemented with innovative GI-EUVR measurements near the Boron edge. A proof of reliability is the fact that $(\text{Interlayer\_01}_{\text{SEM}}\ /\text{Interlayer\_01}_{\text{GI-EUVR}})$ is exactly same as $(\text{Interlayer\_02}_{\text{SEM}}\ /\text{Interlayer\_02}_{\text{GI-EUVR}})$, see column 5 of table 6. This implies robust sensitivity of the method (GI-EUVR + GA) to resolve the effective ("real") optical boundaries throughout the ML structure.

4. CONCLUSION

Multilayers of B4C/CeO2 for the 6.x nm EUV lithography application are fabricated for the first time. DC magnetron sputtering and e-beam evaporation are suitable deposition methods for the fabrication of multilayer coatings. Several experimental techniques are utilized to characterize optical and structural parameters of the MLs. EUV reflection measurements to determine optical properties of MLs were performed at the ELTTRA Synchrotron, Trieste. XRR measurement at $CuK_{\alpha 1}$ for thickness reconstruction was also performed for thickness determination. GI-EUVR analysis has been used for the first time to determine ML parameters.

Performance of the ML at 6.9 nm wavelength and 10° incidence angle from normal is 4.4 times less than the theoretical value. However, this performance is comparable to the leading candidate ML (i.e. La/B) for 6.x nm EUVL with same design parameter [26]. The major cause for such low reflectivity performance is found to be inter-diffusion between layers while uncertainties in tabulated values of optical constants near Boron edge could affect the comparison of between measured and theoretical reflectivity. The High resolution SEM and TEM images also show asymmetry of interdiffusion where CeO2 diffuses deeper and stronger into B4C layer than B4C does into CeO2.

An innovative at-wavelength metrology for optical and structural analysis of MLs near the absorption edge of the spacer-layer element is implemented here for the first time. A numerical fit to this GI-EUVR measured data reconstruct parameters in much accurate and reliable way as shown in Table 5. Its robustness lies in the fact that both optical and structural parameters can be derived, within acceptable range of uncertainties, without a need to combine it with XRR. Further research activities focus on experimental derivation of optical constants of CeO2 from several measurements, and implementation of diffusion barrier techniques in order to increase reflectivity performance at 6.x nm.

ACKNOWLEDGEMENT

The writers acknowledge financial support from the EU FP7 Erasmus Mundus Joint Doctorate Programme EXTATIC under framework partnership agreement FPA-2012-0033.This work was also performed under the support of STSM COST Action MP1203. We also thank Dr. Elmar Neumann of the PGI-8-PT group in the Research Centre Jülich for making the SEM images. Special gratitude to the group of Prof. Wang Zhanshan of Tonji University for making the MLs Samples.

REFERENCES

[1] S. Vitta, M. Weisheit, T. Scharf, and H. U. Krebs, "Alloy-ceramic oxide multilayer mirrors for water-window soft x rays," Optics Letters 26, 1448-1450 (2001).
[2] Y. Uspenskii, D. Burenkov, T. Hatano, and M. Yamamoto, "Optimal design of multilayer mirrors for water-window microscope optics," Optical Review 14, 64-73 (2007).
[3] D. Martinez-Galarce, R. Soufli, D. L. Windt, M. Bruner, E. Gullikson, S. Khatri, E. Spiller, J. C. Robinson, S. Baker, and E. Prast, "Multisegmented, multilayer-coated mirrors for the Solar Ultraviolet Imager," Optical Engineering 52 (2013).
[4] R. J. Matyi, "HIGH RESOLUTION X-RAY REFLECTOMETERY: THEORY, PRACTICE, ACCURACY AND PRECISION," in Analytical and Diagnostic Techniques for Semiconductor Materials and Devices(National Institute of Standards and Technology, Gaithersburg, USA, 2003).
[5] J. Hirase, "Verification of Moore's Law Using Actual Semiconductor Production Data," Ieice Transactions on Electronics E97C, 599-608 (2014).
[6] T. Kozawa, J. J. Santillan, and T. Itani, "Feasibility study of sub-10-nm half-pitch fabrication by chemically amplified resist processes of extreme ultraviolet lithography: I. Latent image quality predicted by probability density model," Japanese Journal of Applied Physics 53 (2014).
[7] S. Wurm, Transition to EUV lithography (2012).
[8] T. G. Oyama, T. Takahashi, A. Oshima, M. Washio, and S. Tagawa, "Extendibility of EUV resists in the exposure wavelength from 13.5 down to 3.1 nm for next-generation lithography," Advances in Resist Materials and Processing Technology Xxviii 7972 (2011).
[9] N. I. Chkhalo, S. Kuenstner, V. N. Polkovnikov, N. N. Salashchenko, F. Schaefers, and S. D. Starikov, "High performance La/B4C multilayer mirrors with barrier layers for the next generation lithography," Applied Physics Letters 102 (2013).
[10] Y. Platonov, J. Rodriguez, M. Kriese, E. Gullikson, T. Harada, T. Watanabe, and H. Kinoshita, "Multilayers for next generation EUVL at 6.Xnm," Euv and X-Ray Optics: Synergy between Laboratory and Space Ii 8076 (2011).
[11] I. A. Makhotkin, E. Zoethout, E. Louis, A. M. Yakunin, S. Muellender, and F. Bijkerk, "Spectral properties of La/B - based multilayer mirrors near the boron K absorption edge," Optics Express 20, 11778-11786 (2012).
[12] Y. Chung-Jong, K. Euikwoun, and K. Jae-Yong, "Parratt-based and Model-independent X-ray Reflectivity Fitting Procedure for Nanoscale Thin Film Characterization," Journal of Nanoscience and Nanotechnology 11, 4624-4628 (2011).
[13] P. Tripathi, G. S. Lodha, M. H. Modi, A. K. Sinha, K. J. S. Sawhney, and R. V. Nandedkar, "Optical constants of silicon and silicon dioxide using soft X-ray reflectance measurements," Optics Communications 211, 215-223 (2002).
[14] P. Tripathi, and G. S. Lodha, "Optical constant of silicon and silicon dioxide using soft X-ray reflectance measurements (vol 211, pg 215, 2002)," Optics Communications 218, 195-195 (2003).
[15] R. Jirawit, "Design and fabrication of Aperiodic multilayers with broadband reflectance in the Soft X-ray regime", University of Cambridge, 2014.

[16] M. Lampton, B. Margon, and S. Bowyer, "PARAMETER-ESTIMATION IN X-RAY ASTRONOMY," Astrophysical Journal 208, 177-190 (1976).
[17] A. Ulyanenkov, K. Omote, and J. Harada, "The genetic algorithm: refinement of X-ray reflectivity data from multilayers and thin films," Physica B 283, 237-241 (2000).
[18] P. D. Binda, and F. E. Zocchi, "Genetic algorithm optimization of X-ray multilayer coatings," in Advances in Computational Methods for X-Ray and Neutron Optics, M. S. DelRio, ed. (2004), pp. 97-108.
[19] I. A. Makhotkin, E. Zoethout, E. Louis, A. M. Yakunin, S. Muellender, and F. Bijkerk, "Wavelength selection for multilayer coatings for lithography generation beyond extreme ultraviolet," Journal of Micro-Nanolithography Mems and Moems 11 (2012).
[20] S. N. Yakunin, I. A. Makhotkin, K. V. Nikolaev, R. W. E. van de Kruijs, M. A. Chuev, and F. Bijkerk, "Combined EUV reflectance and X-ray reflectivity data analysis of periodic multilayer structures," Optics Express 22, 20076-20086 (2014).
[21] M. Nayak, G. S. Lodha, and R. V. Nandedkar, "X-ray reflectivity investigation of interlayer at interfaces of multilayer structures: application to Mo/Si multilayers," Bulletin of Materials Science 29, 693-700 (2006).

[22] S. Nannarone, F. Borgatti, A. DeLuisa, B. P. Doyle, G. C. Gazzadi, A. Giglia, P. Finetti, N. Mahne, L. Pasquali, M. Pedio, G. Selvaggi, G. Naletto, M. G. Pelizzo, and G. Tondello, "The BEAR beamline at ELETTRA," in Synchrotron Radiation Instrumentation, T. Warwick, J. Arthur, H. A. Padmore, and J. Stohr, eds. (2004), pp. 450-453.
[23] D. L. Windt, "IMD, Version 5, Installation and User's Manual," (2013).
24] J. Serafinczuk, J. Pietrucha, G. Schroeder, and T. P. Gotszalk, "Thin film thickness determination using X-ray reflectivity and Savitzky-Golay algorithm," Optica Applicata 41, 315-322 (2011).
[25] M. N. a. G. S. Lodha, "Optical Response Near the Soft X-Ray Absorption Edges and Structural Studies of Low Optical Contrast System Using Soft X-Ray Resonant Reflectivity," Journal of Atomic,Molecular, and Optical Physics 2011, 23 (2011).
[26] I. A. Makhotkin, E. Zoethout, R. van de Kruijs, S. N. Yakunin, E. Louis, A. M. Yakunin, V. Banine, S. Muellender, and F. Bijkerk, "Short period La/B and LaN/B multilayer mirrors for similar to 6.8 nm wavelength," Optics Express 21, 29894-29904 (2013).
[27] S. Roy, and B. N. Dev, "X-ray standing waves in a multi-trilayer system with linearly varying period," Applied Surface Science 257, 7566-7572 (2011).
[28] H. Zenghu, L. Geyang, T. Jiawan, and G. Mingyuan, "Microstructure and mechanical properties of boron carbide thin films," Materials Letters 57, 899-903 (2002).
[29] G. Monaco, D. Garoli, R. Frison, V. Mattarello, P. Nicolosi, M. G. Pelizzo, V. Rigato, L. Armelao, A. Giglia, and S. Nannarone, "Optical constants in the EUV Soft x-ray (5 divided by 152 nm) spectral range of B4C thin films deposited by different deposition techniques - art. no. 631712," in Advances in X-Ray/EUV Optics, Components, and Applications, A. M. Khounsary, and C. Morawe, eds. (2006), pp. 31712-31712.
[30] D. Spiga, A. Mirone, G. Pareschi, R. Canestrari, V. Cotroneo, C. Ferrari, C. Ferrero, L. Lazzarini, and D. Vernani, "Characterization of multilayer stack parameters from X-ray reflectivity data using the PPM program: measurements and comparison with TEM results - art. no. 626616," in Space Telescopes and Instrumentation II: Ultraviolet to Gamma Ray, Pts 1 and 2, M. J. L. Turner, and G. Hasinger, eds. (2006), pp. 26616-26616.
[31] H. Li, J. Zhu, Z. Wang, Z. Song, and H. Chen, "Asymmetrical diffusion at interfaces of Mg/SiC multilayers," Optical Materials Express 3, 546-555 (2013).